

1 **P-wave Reflectivity of the Crust and Upper Mantle Beneath the Southern**
2 **Appalachians and Atlantic Coastal Plain using Global Phases**

3
4 Devon N. Verellen¹, Erik C. Alberts², Gustavo A. Larramendi, E. Horry Parker, Jr.³, and Robert
5 B. Hawman

6
7 Department of Geology, University of Georgia, Athens, GA, USA

8
9 ¹now at Chevron, Houston TX

10 ²now at Exxon/Mobil, Houston, TX

11 ³now at Black & Veatch, Greenville, SC

12
13 **KEY POINTS**

- 14
15 - P-wave reflections generated using PKPdf as a virtual source are observed over depths from 1
16 km to greater than 200 km.
17 - Reflection times reach 17.4 s (> 55 km) for the highest elevations, supporting previous evidence
18 that the southern Appalachians are in isostatic equilibrium.
19 - Reflections at 32-36 s (120-135 km) may indicate drag-induced flow at the base of the
20 lithosphere. These arrivals are observed for single as well as stacked events.
21

22 **INDEX TERMS**

- 23 - Seismology
24 - Tectonophysics

25
26 **KEYWORDS**

- 27 - southern Appalachians, Atlantic Coastal Plain, PKPdf, PKIKP, Moho, LAB

28
29 **PLAIN LANGUAGE SUMMARY**

30
31 The main goal of this work was to study the nature of the boundary between the tectonic plate
32 beneath the southern Appalachians and the underlying, more fluid mantle. We used echo
33 soundings to determine the depth and physical characteristics of major layers. Our strategy was
34 to use seismic waves generated by earthquakes on the opposite side of the planet as an energy
35 source. We see a major transition at depths of 120-135 km that we interpret as drag-induced flow
36 just beneath the plate. We also see evidence for a thickening of Earth's crust beneath the highest
37 elevations of the southern Appalachians that suggests that these very old mountains are in
38 gravitational equilibrium.
39

40 **Abstract**

41
42 Reflection profiles generated using PKPdf as a virtual source show laterally continuous
43 reflections from structures at depths less than 1 km to roughly 200 km beneath the southern
44 Appalachian orogen and Atlantic Coastal Plain. Arrivals interpreted as reflections from the Moho
45 increase in time from ~10 s beneath the Coastal Plain to 17.4 s (~57 km) beneath the Blue Ridge
46 Mountains, providing additional evidence that the southern Appalachians are in rough isostatic
47 equilibrium. Reflections at 32-36 s (120-135 km) are consistent with the depth to the base of the
48 lithosphere found in recent inversions of Ps arrivals and surface waves. Alternatively, these and
49 later reflections at times up to 58 s (~224 km) may be due to layering associated with drag-

50 induced flow in the asthenosphere, suggesting largely horizontal rather than vertical flow for
51 depths less than 225 km beneath the Georgia coastal plain.

52

53 **1. Introduction**

54

55 The passage of USArray across the eastern United States has resulted in fundamentally new
56 insights into the fine-scale structure of the continental lithosphere. Recent analyses of
57 Transportable Array (TA) data for upper mantle structure, including body-wave and surface-wave
58 tomography and analyses of shear-wave splitting, indicate that the lithosphere thins from a
59 maximum of 200-250 km beneath the North American craton [Yuan *et al.*, 2014] to roughly 150
60 km beneath the Grenville Front and Appalachian Mountains (Valley & Ridge and Blue Ridge), to
61 less than 100 km beneath portions of the SE Atlantic Coastal Plain [Pollitz and Mooney, 2016;
62 Shen and Ritzwoller, 2016; Savage *et al.*, 2017]. Analyses of shear-wave splitting generally show
63 fast axes parallel to absolute plate motion (APM) beneath the craton [Yuan *et al.*, 2014; Long *et al.*,
64 *et al.*, 2016; Yang *et al.*, 2017] with more complex patterns eastward toward the continental margin.

65

66 These patterns have been interpreted using a variety of models. For instance, fast axes parallel to
67 the belt of highest elevations in the Appalachian Orogen are also roughly parallel to APM; they
68 have been interpreted both as evidence for strain associated with Alleghanian collision frozen into
69 the lithosphere [Long *et al.*, 2016] and as simple shear generated just above and below the
70 lithosphere-asthenosphere boundary (LAB) by ongoing plate motion [Yang *et al.*, 2017]. Beneath
71 the southeastern U.S. coastal plain, interpretations of a broad zone of null [Long *et al.*, 2016] or
72 small [Yang *et al.*, 2017] splitting times include vertical flow in the asthenosphere (possibly a
73 consequence of edge-driven convection driven by an abrupt transition in lithospheric thickness)
74 [Long *et al.*, 2016; Savage *et al.*, 2017] combined with weak or spatially incoherent anisotropy in
75 the lithosphere. An alternative model involves cancellation of the effects of APM-parallel flow
76 within the broad lithosphere-asthenosphere transition zone by roughly N-S directed flow in the
77 asthenosphere diverted around the keel of the craton [Yang *et al.*, 2017].

78

79 Vertical incidence reflection profiling has the potential to help resolve some of these issues by
80 tracking the lateral continuity of structures within the uppermost mantle. Several large-scale,
81 active-source experiments across Eurasia have been able to detect coherent reflections at normal
82 incidence in the mantle to depths greater than 200 km using large explosions [Knapp *et al.*, 1996;
83 Steer *et al.*, 1998]. In this study, we use the global seismic phase PKIKP (PKPdf) as a virtual
84 source [Ruigrok and Wapenaar, 2012] to construct normal-incidence reflection sections that are
85 analogous to those produced by active-source reflection profiling of the crust. The strategy for
86 this work is to take advantage of the relatively dense station spacing of the broadband arrays
87 deployed during the Southeastern Suture of the Appalachian Margin experiment (SESAME)
88 (Figure 1) [Parker *et al.*, 2013] to investigate P-wave reflectivity or "fabric" over a portion of the
89 upper mantle for which the long-wavelength velocity and anisotropy structure are well
90 constrained by recent analyses of TA data.

91

92 **2. Geologic and Tectonic Setting**

93

94 The southern Appalachians (Figure 1) are the product of diachronous, largely oblique collision of
95 Laurentia with Gondwana and a number of continental fragments and island arcs [Hatcher, 1989,
96 2002, 2010; Hatcher *et al.*, 2007], beginning ~480 Ma and culminating in the Alleghanian
97 orogeny (330-260 Ma). Detachment faults imaged by the Consortium for Continental Reflection
98 Profiling (COCORP) indicate that late Alleghanian collision drove rocks of the Carolina terrane,

99 Inner Piedmont, and Blue Ridge several hundred km to the northwest [*Cook and Vasudevan,*
100 2006; *Duff and Kellogg,* 2017].

101
102 Rifting of the orogen began in the late Triassic, followed by seafloor spreading and opening of
103 the Atlantic by 180 Ma. Beneath Line E, rift basin sediments are restricted to the north end,
104 where they are less than 2500 m thick, but are more extensive beneath Line W where they reach
105 thicknesses of 1000-6000 m [*McBride,* 1991]. Subsequent variations in sea level are recorded in
106 the Atlantic Coastal Plain of Georgia and Florida as a sequence of poorly consolidated Cretaceous
107 and Cenozoic carbonates and siliciclastics up to 2000 m thick [*Chowns and Williams,* 1983].

108

109 **3. Using PKPdf/PKiKP to image P-wave reflectivity**

110

111 The method used in this study is a modification of an approach known as global phase seismic
112 interferometry or “GloPSI” [*Ruigrok & Wapenaar,* 2012]. This approach uses PKiKP (referred
113 to in the rest of this discussion as PKPdf) and PKiKP phases as virtual seismic sources for
114 generating P-wave reflections from the crust and upper mantle. In contrast with other methods
115 for seismic imaging such as receiver functions, GloPSI uses only the vertical component of
116 ground motion. Upon reflection from the earth’s surface, these phases reverse polarity and
117 propagate downward as plane waves with near-vertical raypaths. Therefore they preferentially
118 image structure with small dips.

119

120 **3.1. Processing**

121

122 Most previous analyses of PKPdf/PKiKP (e.g., *Ruigrok and Wapenaar,* 2012) have taken
123 advantage of the equivalence of the P-wave reflection response (the wavefield recorded for a
124 coincident source and receiver) to the positive lags of the autocorrelation of the transmission
125 response (the wavefield recorded at the surface for a source below the depth range of interest)
126 [*Claerbout,* 1968]. Unfortunately, in the absence of large numbers of earthquakes for stacking,
127 the lags of the autocorrelation corresponding to the early part of the output section tend to be
128 dominated by energy associated with the extended source wavelets.

129

130 We try a different approach based on deconvolution of traces prior to stacking using an estimate
131 of the source wavelet for each earthquake. We combine traces from the three profiles (D, W, E)
132 into a single gather and then align first (PKPdf) arrivals by cross correlation. This provides a
133 common time base with the time of the deconvolved first arrival serving as the origin time of
134 reflections. This approach is similar to the method employed by Langston and Hammer [2001]
135 and Yang et al. [2012] for the analysis of teleseismic waves. Following those authors, we
136 estimate source wavelets by stacking seismograms for stations deployed on bedrock, north of the
137 Coastal Plain. The assumption is that lateral variations in structure lead to cancellation of
138 reflections, leaving only the common source wavelet of the earthquake.

139

140 This approach can be complicated by the arrival of two phases (PKPdf and PKiKP) in the time
141 window of interest. For a source depth of 100 km and distances of 115°-140°, travel times for the
142 two phases differ by ~ 0-3 s and ray parameters differ by 0.01–0.26 s/°. Free-surface reflections
143 (pPKPdf and pPKiKP) in the source region have ray parameters that are nearly identical to those
144 for the corresponding arrivals PKPdf and PKiKP. For the earthquakes used in this study, the
145 effective array apertures for stations deployed north of the Coastal Plain ranged from 1.7°–2.6°
146 and the differential moveouts ranged from 0.1-0.4 s. The stacking procedure described above
147 treats all these phases as a single arrival and therefore yields an effective source wavelet of
148 extended duration, with some loss of resolution at higher frequencies. Differential moveouts for
149 PKPdf and PKiKP between those stations and the southernmost stations range from 0.1-1.1 s; this

150 causes some broadening of deconvolved waveforms that is minimized by stacking (Figures S8-
151 S9).

152

153 Over the distance range 115°-145°, interference from PP, which follows PKPdf by 60 – 180 s, is
154 largely avoided, but earthquakes in the distance range 145°-155° are not included in the analysis
155 because of interference with the phases PKPab and PKPbc. Scattering by lateral heterogeneities
156 near the base of the mantle can also contaminate the record [Hedlin *et al.*, 1997]; this situation is
157 flagged by coherent energy arriving shortly before PKPdf. Beyond 160°, PKPdf and PKPab
158 diverge rapidly, but the listening window is restricted by PKP_{diff}, the diffraction along the
159 inner/outer core boundary, which follows PKPdf by 14-34 s.

160

161 **3.2 Results**

162

163 Deconvolution was carried out in the frequency domain. We used a water-level value of 0.0001
164 to stabilize spectral division and a range of Gaussian functions ($\alpha = 1.0 - 4.0$) to smooth the
165 output waveforms [Langston, 1979]. Deconvolved gathers for single earthquakes were stacked to
166 suppress noise (both random and coherent) and to enhance signal levels. Prior to stacking, each
167 trace was normalized by the amplitude of the direct PKPdf arrival, then divided by the RMS
168 value of noise 0-18 s prior to PKPdf to give greater weight to seismograms with higher signal
169 levels. After stacking, samples were multiplied by a factor equal to the square root of two-way
170 time to smoothly increase amplitudes of later reflections.

171

172 The deconvolved direct arrival at time zero is assigned a positive polarity. As noted earlier, upon
173 reflection at the earth's surface, this polarity is reversed. Therefore the direct arrival and
174 reflections from positive impedance contrasts (e.g., crust over mantle) will show opposite
175 polarities. The 16 earthquakes used in this study are summarized in Table S1. The resulting
176 stacks (Figures 2-4 and S3-S6) show coherent reflections with dominant periods ranging from 1-4
177 s and from interfaces in the near surface to depths of ~200 km.

178

179 **3.2.1. Coastal Plain Sediments**

180

181 For stations over the Coastal Plain, vertical stacks and many of the records for individual events
182 show a series of strong, coherent reflections 0.2-4.2 s after the direct arrival (Figures 2 and S4).
183 Travel times for the peak of the first half cycle (0.2-1.4 s; opposite in polarity from PKPdf,
184 indicating a positive impedance contrast) match those predicted for reflection from the base of the
185 sequence of Cretaceous and younger sediments and poorly consolidated sedimentary rocks. This
186 event starts very close to the feather edge of the sequence at the northern boundary of the Coastal
187 Plain and increases in travel time to the south, in agreement with thicknesses derived from well
188 data [Chowns and Williams, 1983]. For Line E (Figure S4), travel times are best fit by an
189 average P-wave velocity of 2400 m/s for stations E31 to E25 and by a slightly greater average
190 velocity (2600 m/s) for the thicker sequences beneath stations E24-E07. For Line W (Figure 2),
191 the best fits are obtained for velocities of 2200 m/s for stations W21-W19, 2400 m/s for stations
192 W18-W10, and 2100 m/s for stations W09-W01. These values are consistent with those reported
193 by Iverson and Smithson [1983] and Barnes and Reston [1992].

194

195 Travel times for the later 2-3 half-cycles are consistent with times predicted for free-surface
196 multiples. Travel times for the second multiple bounce overlap those predicted for the base of the
197 underlying Triassic/Jurassic sedimentary sequence; resolution of the latter will require additional
198 deconvolution (work in progress).

199

200 **3.2.2. Moho**

201

202 For Line W, events interpreted as Moho reflections are clearest at lower frequencies ($\alpha=1.0$;
 203 Figure 2). Two-way times vary between 9.7 and 10.1 s for stations W02 to W06 and between
 204 10.0 and 10.9 s for stations W07 and W22, all within the Coastal Plain. Moho reflection times
 205 reported for coincident COCORP lines [McBride, 1991] are somewhat greater (11.2 – 12.0 s),
 206 suggesting that the broader PKPdf-generated waveforms may represent a composite of reflections
 207 from lower crustal layering and the crust-mantle transition itself (work in progress). A similar
 208 result is obtained for Line E (Figure S3). From station W22 the times increase northward, from
 209 12.2 s at station W23 to 12.8 s (crustal thickness: 42 km) at station W31 (Inner Piedmont), with a
 210 pronounced increase from 13.8 s (45 km) at W315 (foothills) to 17.4 s (57 km) beneath W35 in
 211 the Blue Ridge Mountains. A similar trend is observed for Line D (Figure S2). These are the
 212 first observations of normal-incidence P-wave reflections from the Moho beneath the higher
 213 elevations of the southern Appalachians. The results for Lines W and D are consistent with other
 214 broadband and active-source results suggesting that the southern Appalachians are in rough local
 215 isostatic equilibrium [French *et al.*, 2009; Hawman *et al.*, 2012; Schmandt *et al.*, 2015; Parker *et*
 216 *al.*, 2013; 2016; Hopper *et al.*, 2016].

217

218 **3.2.3. Upper Mantle**

219

220 Stacks for Line E show reflections at 16-20 s (depths: 50-75 km; Figures 3 and S4). A similar
 221 reflection sequence is not seen in the stacks for Line W, but reflections in this depth range do
 222 appear in sections derived by pre-stack migration (Figure S10; see below). Models of S-wave
 223 velocity for the southern Appalachian highlands, derived by inversion of surface waves [Savage
 224 *et al.*, 2017], show a low-velocity zone over a similar depth range. Similar “mid-lithospheric
 225 discontinuities” occur throughout the North American craton and are variously interpreted as low-
 226 velocity cumulate layers, refertilized depleted mantle, stacks of oceanic plates, and underplating
 227 [Abt *et al.*, 2010; Calo *et al.*, 2016]. Alternatively, the reflections could be generated by layers
 228 within the uppermost mantle depleted by partial melting during Mesozoic extension [Pollitz &
 229 Mooney, 2016].

230

231 For Lines E and W, multicyclic reflections between 32 s and 36 s are consistent with a layered
 232 zone at depths of 120 - 135 km (Figures 3, 4, S4, S5). This is roughly 30 km deeper than the
 233 lithosphere/asthenosphere boundary (LAB) inferred from analysis of S_p receiver functions for a
 234 nearby broadband station [Abt *et al.*, 2010] but is in better agreement with more recent studies
 235 based on inversion of surface waves [Savage *et al.*, 2017] and joint inversion of surface waves
 236 and P_s receiver functions [Calo *et al.*, 2016].

237

238 The frequency content and multicyclic character of the reflections indicates much smaller
 239 wavelength variations in velocity than expected for a purely thermal boundary. At these depths,
 240 quarter-wavelength estimates of vertical resolution, corresponding to layer thicknesses required
 241 for constructive interference of reflections from multiple layers, range from 3-8 km (Supplement).
 242 This scale of layering would be consistent with models incorporating the effects of shearing at the
 243 transition and also with intrusions triggered by partial melting of hydrated asthenosphere [Fischer
 244 *et al.*, 2010; Till *et al.*, 2010]. Alternatively, these and deeper signals at roughly 44 s (~167 km)
 245 and 58 s (~ 224 km) (Figure 4) may be reflections from layering associated with drag-induced
 246 flow in the asthenosphere [Eaton *et al.*, 2009; Fischer *et al.*, 2010; Long *et al.*, 2016]. The event
 247 at 58 s is close in depth to a transition identified beneath North America as the Lehmann
 248 discontinuity [Calo *et al.*, 2016]; this feature was originally interpreted as the base of a low-
 249 velocity zone [Lehmann, 1960] but could also represent an abrupt decrease in transverse

250 anisotropy marking the base of a zone of strong coupling between asthenosphere and lithosphere
251 [Gaherty and Jordan, 1995; Eaton et al., 2009]. These deeper reflections are consistent with
252 largely horizontal rather than vertical flow at depths less than 225 km beneath this portion of the
253 Georgia Coastal Plain.

254

255 ***3.2.4. Individual Events***

256

257 The above approach is capable of recovering useful signal levels for single earthquakes, even
258 without stacking. Deconvolved records for individual events (Figure 5) show consistent results
259 for earthquakes over a range of magnitudes and focal depths, indicating that major arrivals
260 (particularly those interpreted as reflections from the LAB at 32-36 s) are indeed reflections and
261 not artifacts generated by incomplete deconvolution of source-side scattering and other coherent
262 noise (Figures S6 and S7).

263

264 However, the results for individual earthquakes do show some variations in arrival times and
265 relative amplitudes for major arrivals, which tend to degrade the stacks (e.g., the events at 32-34 s
266 in Figure 4), and also show variations in reflection density over different time windows. We
267 attribute these variations to differences in dominant frequencies for different magnitude
268 earthquakes, processing artifacts, particularly near the end of listening windows (Figure S6 and
269 S7), small-scale lateral heterogeneity, and variations in back-azimuth. To define major structural
270 boundaries, we rely on the stacked images. To preserve a composite image of finer-scale structure
271 or “fabric”, we migrate the deconvolved sections for individual earthquakes separately and stack
272 the results. Preliminary migration results based on a subset of events are presented in the
273 Supporting Information (Figures S10 and S11).

274

275 **4. Conclusions**

276

277 Reflection profiles generated using PKPdf as a virtual seismic source show laterally continuous
278 structures at depths from the near-surface to roughly 200 km beneath the southern Appalachian
279 orogen and adjacent Atlantic Coastal Plain. Waveforms are deconvolved for each earthquake
280 separately, using estimates of the source wavelet derived by stacking over multiple stations. The
281 results for multiple earthquakes then are stacked to form composite images of the crust and
282 uppermost mantle.

283

284 The profiles show clear, continuous signals with times in close agreement with those expected for
285 primary and multiple reflections from the base of coastal plain sediments. Arrivals interpreted as
286 reflections from the Moho increase in travel time from ~10 s beneath the Coastal Plain to 17.4 s
287 (~57 km) beneath the Blue Ridge Mountains, in agreement with trends observed for wide-angle
288 reflections and Ps and Sp arrivals, and provide additional evidence that the Appalachian
289 highlands are in rough isostatic equilibrium. Reflections at 16-20 s (50-75 km) beneath the
290 coastal plain are consistent with layering associated with depletion of the uppermost mantle
291 during Triassic rifting. Reflections at 32-36 s (120-135 km) are roughly 30 km deeper than
292 previous estimates of LAB depth based on Sp receiver functions, but are consistent with the depth
293 to the LAB found in more recent inversions of Ps arrivals and surface waves. Alternatively, these
294 and later reflections at roughly 44 s (~167 km) and 58 s (~224 km) may be due to layering
295 associated with drag-induced flow in the asthenosphere, suggesting largely horizontal rather than
296 vertical flow for depths less than 225 km beneath the Georgia coastal plain.

297

298

299

300

301 **Acknowledgements**

302

303 D. N. Verellen was supported by a Chevron research assistantship. We thank our SESAME co-
 304 PIs, K. M. Fischer and L. S. Wagner, for helpful discussions, P. Miller, N. Barstow, and G. Slad
 305 of the PASSCAL Instrument Center for assistance in the field, our broadband station hosts, and
 306 the members of our field crew. This work was supported by the Joseph W. Berg fund and by
 307 National Science Foundation grants EAR-0844154 and EAR-1830182.

308

309 **Data Sources**

310

311 The waveform data used for this study can be accessed from the IRIS Data Management Center at
 312 <http://www.iris.edu/SeismiQuery>. The network code for the SESAME experiment is “Z9”. IRIS
 313 Data Services are funded through the Seismological Facilities for the Advancement of
 314 Geoscience (SAGE) Award of the National Science Foundation under Cooperative Support
 315 Agreement EAR-1851048.

316

317 **References**

318

319 Abt, D. L., K. M. Fischer, S. W. French, H. A. Ford, H. Yuan, and B. Romanowicz (2010), North
 320 American lithosphere discontinuity structure imaged by Ps and Sp receiver functions, *J.*
 321 *Geophys. Res.*, *115*, doi:10.1029/2009JB006914.

322 Barnes A. E., and T. J. Reston (1992), A study of two mid-crustal bright spots from southeast
 323 Georgia (USA), *Geophys. J. Int.*, *108*, 683-691.

324 Calo, M., T. Bodin, and B. Romanowicz (2016), Layered structure in the upper mantle across
 325 North America from joint inversion of long and short period seismic data, *Earth &*
 326 *Planetary Science Letters*, *449*, 164-175, doi:10.1016/j.epsl.2016.05.054.

327 Chowins, T. M. and C. T. Williams (1983), Pre-Cretaceous rocks beneath the Georgia Coastal
 328 Plain – Regional implications, in Studies related to the Charleston, South Carolina,
 329 earthquake of 1886 – Tectonics and Seismicity, *Geol. Surv. Prof. Paper 1313-L*, 42 pp.,
 330 U. S. Geol. Survey, Washington, D.C.

331 Claerbout, J. (1968), Synthesis of a layered medium from its acoustic transmission response,
 332 *Geophysics*, *33*, 264-269.

333 Cook, F. A., and K. Vasudevan (2006), Reprocessing and enhanced interpretation of the initial
 334 COCORP southern Appalachian traverse, *Tectonophysics*, *420*, 161-174.

335 Duff, P. D., and J. N. Kellogg (2017), Reinterpretation of ADCOH and COCORP seismic
 336 reflection data with constraints from detailed forward modeling of potential field data –
 337 Implications for Laurentia-Peri-Gondwana suture, *Tectonophysics*, *712-713*, p. 426-437.

338 Eaton, D. W., F. Darbyshire, R. L. Evans, H. Grutter, A. G. Jones, and X. Yuan (2009), The
 339 elusive lithosphere-asthenosphere boundary (LAB) beneath cratons, *Lithos*, *109*, 1-22,
 340 doi:10.1016/j.lithos.2008.05.009.

341 Fischer, K. M., H. A. Ford, D. L. Abt, and C. A. Rychert (2010), The lithosphere-asthenosphere
 342 boundary, *Ann. Rev. Earth Planet. Sci.*, *38*, 551-575, doi:10.1146/annurev-earth-040809-
 343 152438.

344 French, S. W., K. M. Fischer, E. M. Syracuse, and M. E. Wysession (2009), Crustal structure
 345 beneath the Florida-to-Edmonton broadband seismometer array, *Geophys. Res. Lett.*, *36*,
 346 L08309, doi:10.1029/2008GL036331.

347 Gaherty, J. B. and T. H. Jordan (1995), Lehmann discontinuity as the base of an anisotropic layer
 348 beneath continents, *Science*, *268*, 1468-1471.

349 Hansen, K. M., K. Roy-Chowdhury, and R. A. Phinney (1988), The sign filter for seismic event
 350 detection, *Geophysics*, *53*, 1024-1033.

- 351 Hatcher, R. D., Jr. (1989), Tectonic synthesis of the U. S. Appalachians, in Hatcher, R. D., Jr.,
 352 Thomas, W. A., and Viele, G. W., eds., The Appalachian-Ouachita Orogen in the United
 353 States, Geological Society of America, The Geology of North America, v. F-2, p. 511-
 354 535.
- 355 Hatcher, R. D., Jr. (2002), The Alleghanian (Appalachian) orogeny, a product of zipper tectonics:
 356 Rotational transpressive continent-continent collision and closing of ancient oceans along
 357 irregular margins, in Martinez Catalan, J. R., Hatcher, R. D., Jr., Arenas, R., and Garcia,
 358 F. D., eds., Variscan-Appalachian Dynamics: The Building of the Late Paleozoic
 359 Basement, Geological Society of America Special Paper 394, p. 199-208.
- 360 Hatcher, R. D., Jr. (2010), The Appalachian orogeny: A brief summary, in *From Rodinia to*
 361 *Pangea: the Lithotectonic Record of the Appalachian Region*, *Geol. Soc. Am. Mem.* 206,
 362 edited by R. P. Tollo et al., pp. 1-19. GSA, Boulder, CO.
- 363 Hatcher, R. D., Jr., Bream, B. R., and Merschat A. J. (2007), Tectonic map of the southern and
 364 central Appalachians: A tale of three orogens and a complete Wilson cycle, in Hatcher,
 365 R. D., Jr., Carlson, M. P., McBride, J. H., and Martinez Catalan, J. R., eds., 4-D
 366 Framework of Continental Crust, Geological Society of America Memor 200, p. 595-632.
- 367 Hawman, R. B. (2008), Crustal thickness variations across the Blue Ridge Mountains, southern
 368 Appalachians: An alternative procedure for migrating wide-angle reflection data, *Bull.*
 369 *Seismol. Soc. Am.*, 98, 469-475, doi:10.1785/0120070027.
- 370 Hawman, R. B., M. O. Khalifa, and M. S. Baker (2012), Isostatic compensation for a portion of
 371 the southern Appalachians: Evidence from a reconnaissance study using wide-angle,
 372 three-component seismic soundings, *Geol. Soc. Am. Bull.*, 124, 291-317,
 373 doi:10.1130/B30464.1.
- 374 Hedlin, M. A., P. M. Shearer, and P. S. Earle (1997), Seismic evidence for small-scale
 375 heterogeneity through the Earth's mantle, *Nature*, 387, 145-150.
- 376 Hopper, E., K. M. Fischer, S. Rondenay, R. B. Hawman, and L. S. Wagner (2016), Imaging
 377 crustal structure beneath the southern Appalachians with wavefield migration, *Geophys.*
 378 *Res. Lett.*, doi:10.1002/2016GL071005.
- 379 IRIS Data Management Center, Incorporated Research Institutions for Seismology,
 380 <http://www.iris.edu/SeismiQuery>.
- 381 Iverson, W. P., and S. B. Smithson (1983), Reprocessing and reinterpretation of COCORP
 382 southern Appalachian profiles, *E. and Planet. Sci. Lett.*, 62, 75-90, doi:10.1016/0012-
 383 821X(83)90072-9.
- 384 King, P. B. (1961), Systematic pattern of Triassic dikes in the Appalachian region, U. S.
 385 Geological Survey Professional Paper 424-B, B93-B95.
- 386 Knapp, J. H., D. N. Steer, L. D. Brown, R. Berzin, A. Suleimanov, M. Stiller, E. Luschen, D. L.
 387 Brown, R. Bulgakov, S. N. Kashubin, and A. V. Rybalka (1996), Lithosphere-scale
 388 seismic image of the southern Urals from explosion-source reflection profiling, *Science*,
 389 274, 226-228.
- 390 Langston, C.A. (1979), Structure under Mount Ranier, Washington, inferred from teleseismic
 391 body waves, *J. Geophys. Res.*, 84, 4749-4762.
- 392 Langston, C. A. and J. K. Hammer (2001), The vertical component P-wave receiver function,
 393 *Bull. Seismol. Soc. Am.*, 91, 1805-1819.
- 394 Lehmann, I. (1960), Structure of the upper mantle as derived from the travel times of seismic P
 395 and S waves, *Nature*, 186, 956.
- 396 Long, M. D., K. G. Jackson, and J. F. McNamara (2016), SKS splitting beneath Transportable
 397 Array stations in eastern North America and the signature of past lithospheric
 398 deformation, *Geochem. Geophys. Geosyst.*, 17, 2-15, doi:10.1002/2015GC006088.
- 399 Marzen, R. E., D. J. Shillington, D. Lizarralde, and S. H. Harder (2019), Constraints on
 400 Appalachian orogenesis and continental rifting in the southeaster United States from
 401 wide-angle seismic data, *J. Geophys. Res.*, 124, 6625-6652, doi:10.1029/2019JB017611.

- 402 McBride, J. H. (1991), Constraints on the structure and tectonic development of the early
403 Mesozoic South Georgia Rift, southeastern United States: Seismic reflection data
404 processing and interpretation, *Tectonics*, *10*(5), 1065-1083, doi: 10.1029/90tc02682.
- 405 McBride, J. H., K. D. Nelson, and L. D. Brown (1989), Evidence and implications of an extensive
406 early Mesozoic rift basalt/diabase sequence beneath the southeast Coastal Plain, *Geol.*
407 *Soc. Am. Bull.*, *101*, 512-520.
- 408 Milkereit, B. (1987), Migration of noisy crustal seismic data, *J. Geophys. Res.*, *92*, 7916-7930.
- 409 Neidell, N. S. and M. T. Taner (1971), Semblance and other coherency measures for multichannel
410 data, *Geophysics*, *36*, 482-497.
- 411 Parker, E. H., Jr., R. B. Hawman, K. M. Fischer, and L. S. Wagner (2013), Crustal evolution
412 across the southern Appalachians: Initial results from the SESAME broadband array,
413 *Geophys. Res. Lett.*, *40*, 3853-3857, doi:10.1002/grl.50761.
- 414 Parker, E. H., Jr., R. B. Hawman, K. M. Fischer, and L. S. Wagner (2015), Constraining
415 lithologic variability along the Alleghagian detachment in the southern Appalachians
416 using passive-source seismology, *Geology*, *43*, 431-434, doi: 10.1130/G36517.1.
- 417 Parker, E. H., R. B. Hawman, K. M. Fischer, and L. S. Wagner (2016), Estimating crustal
418 thickness using SsPmp in regions covered by low-velocity sediments: Imaging the Moho
419 beneath the Southeastern Suture of the Appalachian Margin Experiment (SESAME)
420 array, SE Atlantic Coastal Plain, *Geophys. Res. Lett.*, *43*, doi:10.1002/2016GL070103.
- 421 Phinney, R. A. and D. M. Jurdy (1979), Seismic imaging of deep crust, *Geophysics*, *44*, 1637-
422 1660.
- 423 Pollitz, F. F. and W. D. Mooney (2016), Seismic velocity structure of the crust and shallow
424 mantle of the Central and Eastern United States by seismic surface wave imaging,
425 *Geophys. Res. Lett.*, *43*, 118-126, doi:10.1002/2015GL066637.
- 426 Robinson, E. A. and S. Treitel (1980), *Geophysical Signal Analysis*, Prentice Hall, New York,
427 466 pp.
- 428 Ruigrok, E. and K. Wapenaar (2012), Global-phase seismic interferometry unveils P-wave
429 reflectivity below the Himalayas and Tibet, *Geophys. Res. Lett.*, *39*, L11303,
430 doi:10.1029/2012GL051672.
- 431 Savage, B., B. M. Covellone, and Y. Shen (2017), Wave speed structure of the eastern North
432 American margin, *Earth Planet. Sci. Lett.*, *459*, 394-405, doi: 10.1016/j.epsl.2016.11.028.
- 433 Schmandt, B., F.-C. Lin, and K. E. Karlstrom (2015), Distinct crustal isostasy trends east and
434 west of the Rocky Mountain Front, *Geophys. Res. Lett.*, *42*, doi:10.1002/2015GL066593.
- 435 Shen, W., and M. H. Ritzwoller (2016), Crustal and uppermost mantle structure beneath the
436 United States, *J. Geophys. Res.*, doi: 10.1002/2016JB012887.
- 437 Steer, D. N., J. H. Knapp, L. D. Brown, H. P. Echtler, D. L. Brown, and R. Berzin (1998), Deep
438 structure of the continental lithosphere in an unextended orogen: An explosive-source
439 seismic reflection profile in the Urals (Urals Seismic Experiment and Integrated Studies
440 (URSEIS 1995)), *Tectonics*, *17*, 143-157.
- 441 Stoffa, P. L., P. Buhl, J. B. Diebold, and F. Wenzel (1981), Direct mapping of seismic data to the
442 domain of intercept time and ray parameter: a plane wave decomposition, *Geophysics*,
443 *46*, 255-267.
- 444 Till, C. B., L. T. Elkins-Tanton, and K. M. Fischer (2010), A mechanism for low-extent melts at
445 the lithosphere-asthenosphere boundary, *Geochemistry, Geophysics, Geosystems*, *11*(10),
446 doi:10.1029/2010gc003234.
- 447 Yang, B. B., Y. Liu, H. Dahm, K. H. Liu, and S. S. Gao (2017), Seismic azimuthal anisotropy
448 beneath the eastern United States and its geodynamic implications, *Geophys. Res. Lett.*,
449 *44*, 2670-2678, doi:10.1002/2016GL071227.
- 450 Yang, Z., A. F. Sheehan, W. L. Yeck, K. C. Miller, E. A. Erslev, L. L. Worthington, and S. H.
451 Harder (2012), Imaging basin structure with teleseismic virtual source reflection profiles,
452 *Geophys. Res. Lett.*, *39*, L02303, doi:10.1029/2011GL050035.

- 453 Yu, Y., J. Song, K. H. Liu, and S. S. Gao (2015), Determining crustal structure beneath seismic
454 stations overlying a low-velocity sedimentary layer using receiver functions, *J. Geophys.*
455 *Res. Solid Earth*, *120*, 3208-3218, doi:10.1002/2014JB011610.
- 456 Yuan, H., S. French, P. Cupillard, and B. Romanowicz (2014), Lithospheric expression of
457 geological units in central and eastern North America from full waveform tomography,
458 *Earth and Planet. Sci. Lett.*, *402*, 176-186, doi:10.1016/j.epsl.2013.11.057.
459
460

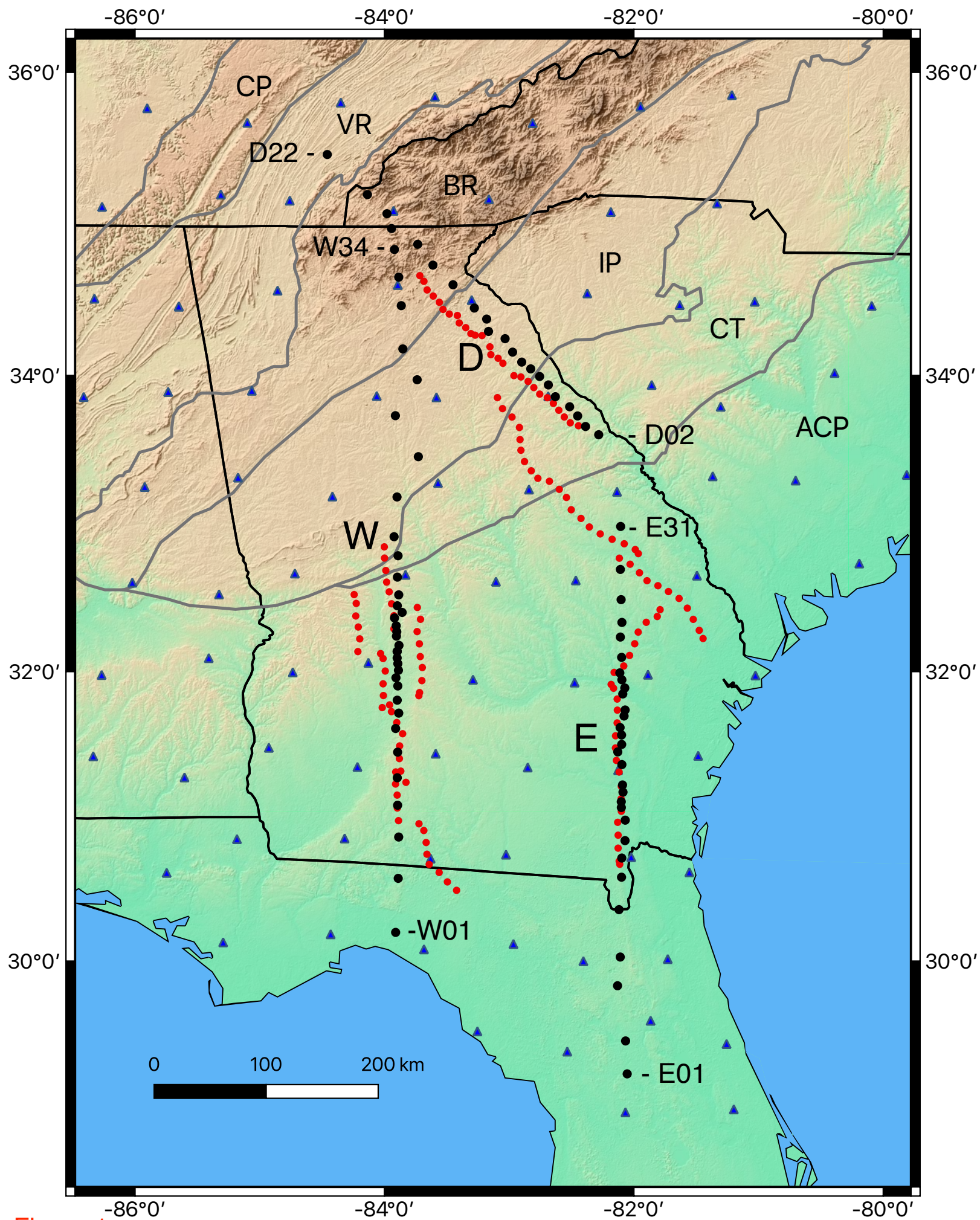


Figure 1

Figure 1. Map of the study area. Blue dots: SESAME stations along lines W, D, and E. Blue triangles: TA stations. Red dots: subset of stations for overlapping COCORP lines.

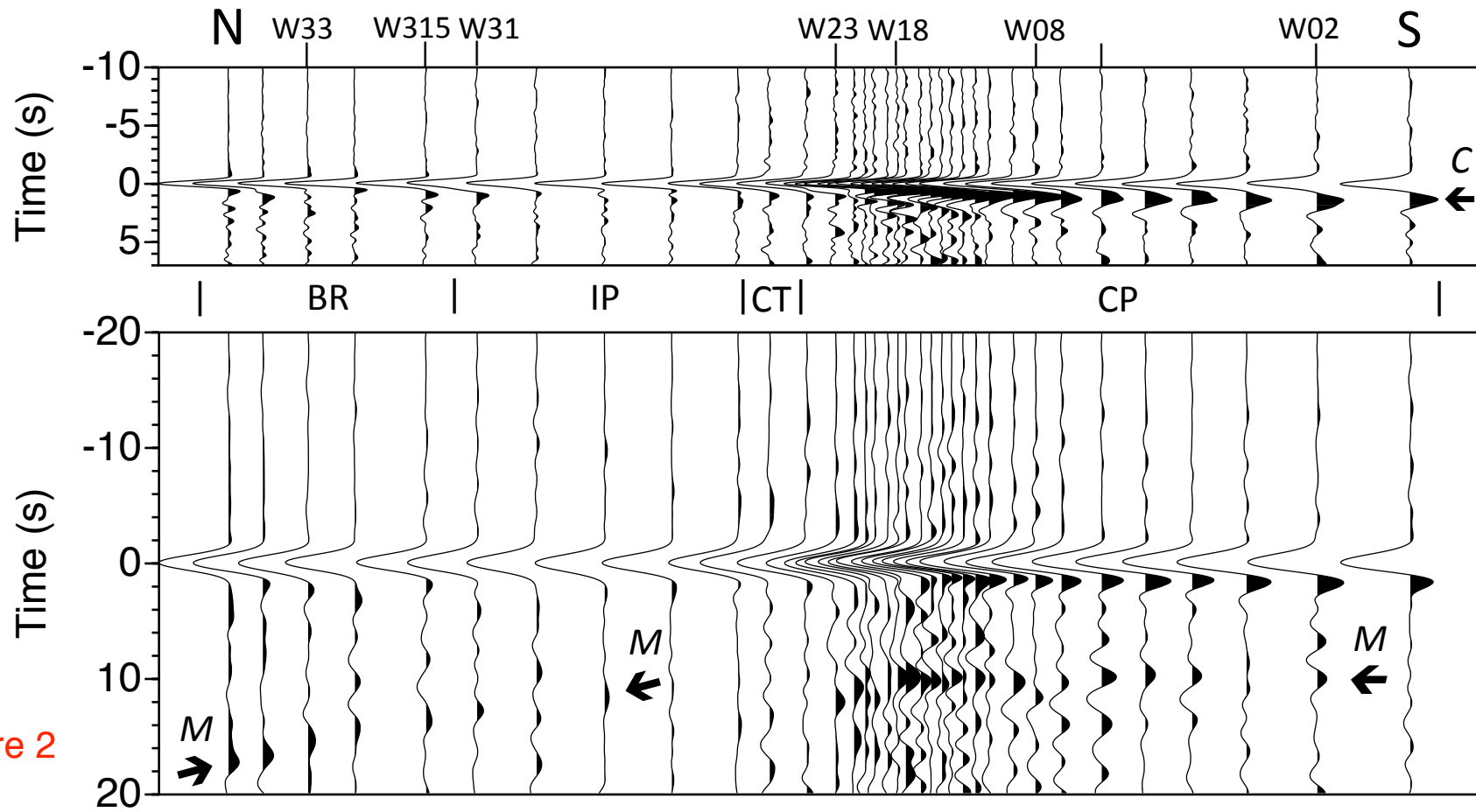


Figure 2

Figure 2. Stacks of deconvolved records for 16 earthquakes (Table S1) showing PKPdf-generated reflections beneath SESAME Line W, using Gaussian smoothing parameters $\alpha=3.0$ (top) and 1.0 (bottom). Plotted with reverse polarity (negative polarity for the direct PKPdf arrival at 0 s). Top: “C” is interpreted as the reflection from the base of Cretaceous-Tertiary sediments and poorly consolidated sedimentary rocks. Times are consistent with well data. This reflection merges with the direct arrival near the northern edge of the Coastal Plain. Bottom: “M” is interpreted as the reflection from the Moho, increasing in two-way time from roughly 10 s beneath the Coastal Plain to 17.5 s beneath the Blue Ridge Mountains. A similar trend in crustal thickness is seen at higher frequencies for Line D (Figure S2).

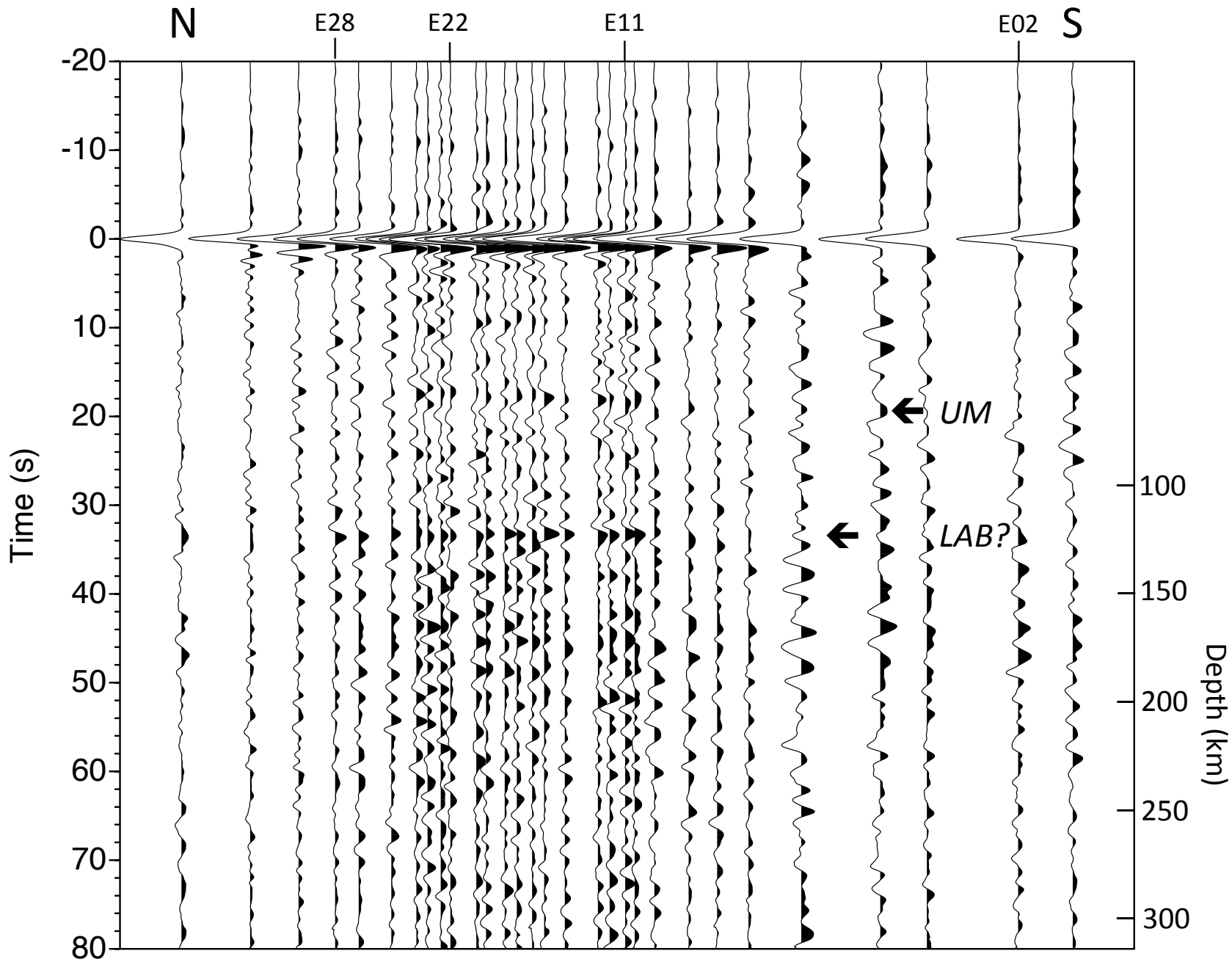


Figure 3

Figure 3. Stack of deconvolved records ($\alpha=2.0$) for 6 earthquakes (Table S1) showing reflections beneath SESAME Line E, plotted with reverse polarity. Depths are approximated using a laterally uniform velocity model (crustal thickness: 55 km; average velocities: 6.5 and 8.1 km/s for the crust and upper mantle, respectively). This approximation contributes 0.5-2.5 km to uncertainties in depth within the mantle. UM: upper mantle reflections. Multicyclic reflections observed at 34–36 s (~127-135 km) may mark the effects of shearing in the vicinity of the LAB and/or intrusions triggered by partial melting of hydrated asthenosphere.

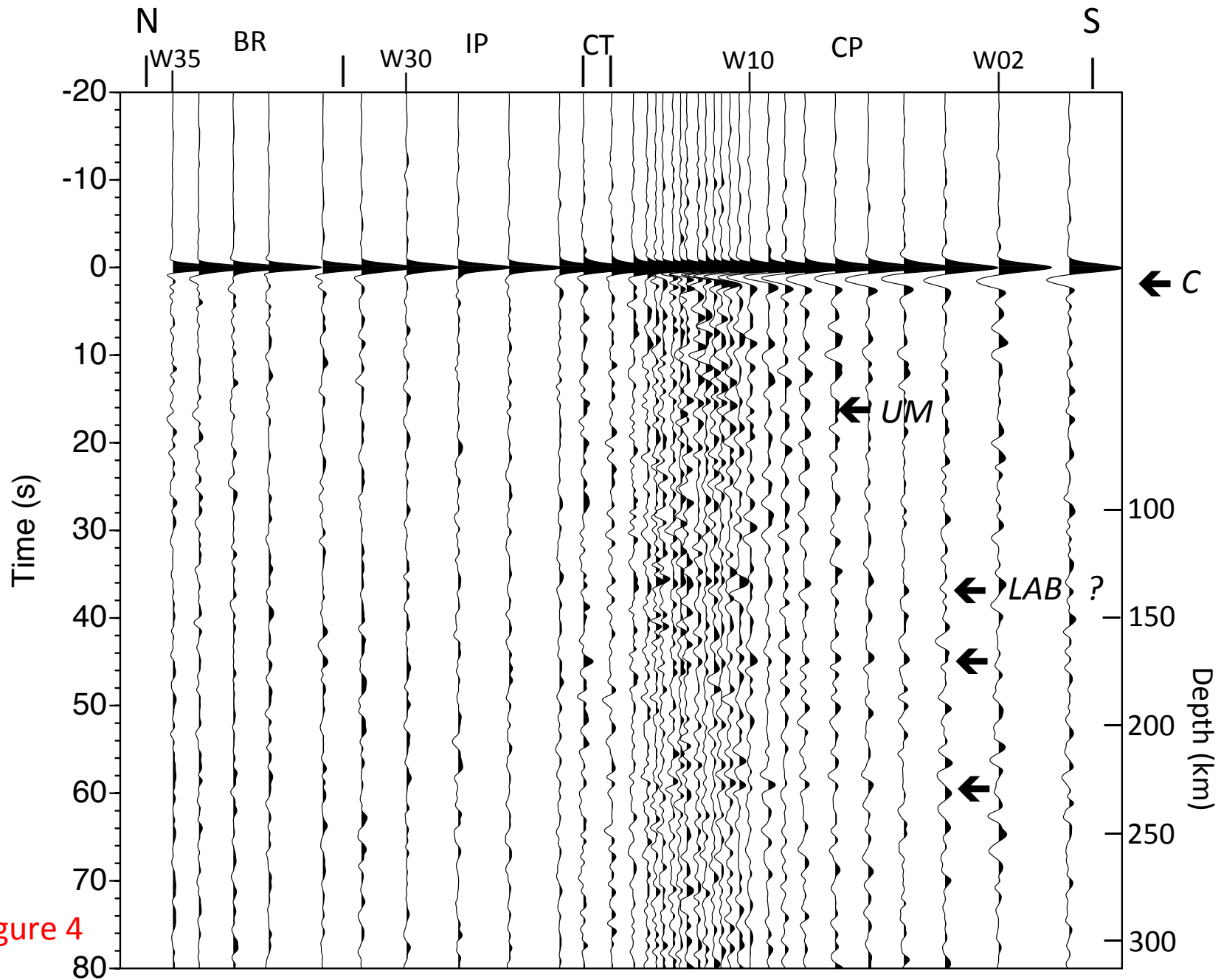


Figure 4. Stack of deconvolved records ($\alpha=2.0$) for 16 earthquakes showing reflections beneath SESAME Line W, plotted with normal polarity (see also Figure S5). C: reflection from the base of Cretaceous and Tertiary sediments and poorly consolidated sedimentary rocks (see also Figure 2). The arrival at 35 s (depth approximately 130 km) is in close agreement with arrivals interpreted as the LAB in Figure 3. Later arrivals at roughly 44 s and 58 s (arrows; ~167 km and 224 km) are interpreted as reflections from layering within the asthenosphere.

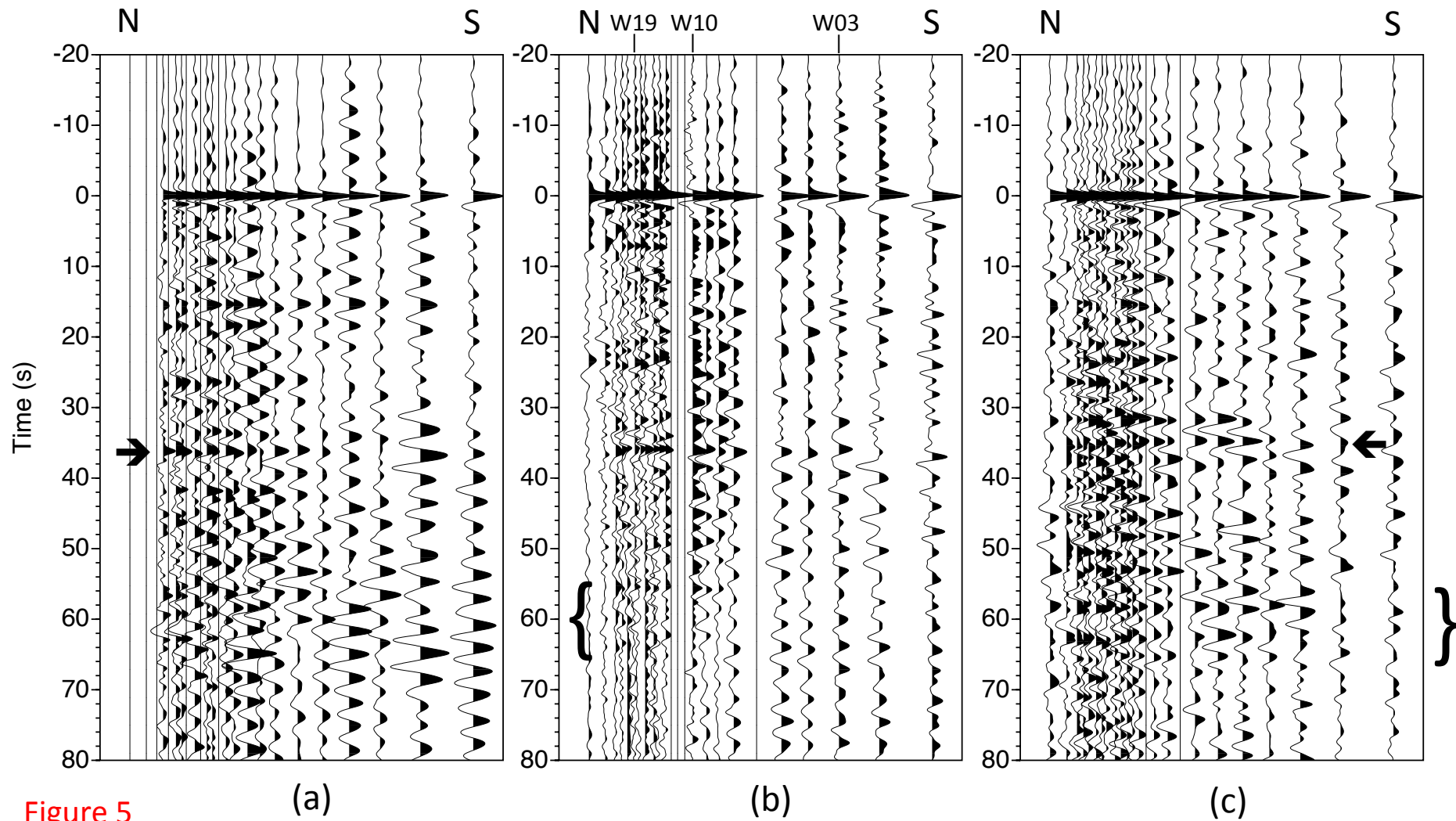


Figure 5

Figure 5. Unstacked, deconvolved sections ($\alpha=2.0$) for the southern half of SESAME Line W, plotted with normal polarity. Note the agreement in travel time for events at approximately 32-36 s (depth: 120-135 km), interpreted in Figure 4 as reflections from the LAB. See also Figures S6 and S7.

(a) Event 1: $M_w=7.3$, depth=386 km, $\Delta = 118^\circ-120^\circ$, back-az = $284^\circ-286^\circ$.

(b) Event 5: $M_w=6.6$, depth=20 km, $\Delta = 125^\circ-127^\circ$, back-az = $290^\circ-293^\circ$.

(c) Event 9: $M_w=6.7$, depth=18 km, $\Delta = 129^\circ-132^\circ$, back-az = $323^\circ-325^\circ$.